

# Twisted nodal wires and three-dimensional quantum spin Hall effect in distorted square-net compounds

Junze Deng,<sup>1,2</sup> Dexi Shao,<sup>1,2,3,\*</sup> Jiacheng Gao,<sup>1,2</sup> Changming Yue,<sup>4</sup> Hongming Weng,<sup>1,2</sup> Zhong Fang,<sup>1,2</sup> and Zhijun Wang<sup>1,2,†</sup>

<sup>1</sup>Beijing National Laboratory for Condensed Matter Physics, and Institute of Physics, Chinese Academy of Sciences, Beijing 100190, China

<sup>2</sup>University of Chinese Academy of Sciences, Beijing 100049, China

<sup>3</sup>Department of Physics, Hangzhou Normal University, Hangzhou 311121, China

<sup>4</sup>Department of Physics, University of Fribourg, 1700 Fribourg, Switzerland

(Dated: December 30, 2021)

Recently, square-net materials [space group (SG)  $P4/nmm$ ] have attracted lots of attention for the Dirac semimetal phase with negligible spin-orbit coupling (SOC) gap, *e.g.*, ZrSiS/LaSbTe and CaMnSb<sub>2</sub>. In this work, we demonstrate that the Jahn-Teller effect enlarges the nontrivial SOC gap in the distorted structure (SG  $Pnma$ ), *e.g.*, LaAsS and SrZnSb<sub>2</sub>. Its distorted  $X$  square-net layer ( $X = \text{P, As, Sb, Bi}$ ) resembles a quantum spin Hall (QSH) insulator. Since these QSH layers are simply stacked in  $\hat{x}$  direction and weakly coupled, three-dimensional QSH effect can be realized in these distorted materials, such as insulating compounds CeAs<sub>1+x</sub>Se<sub>1-y</sub> and EuCdSb<sub>2</sub>. Our detailed calculations show that it hosts two twisted nodal wires without SOC (each consists of two non-contractible  $\mathcal{TI}$ -protected nodal lines touching at a fourfold point), while with SOC it becomes a topological crystalline insulator with symmetry indicators (000;2) and mirror Chern numbers (0,0). The nontrivial band topology is characterized by a generalized spin Chern number  $C_{s+} = 2$  when there is a gap between two sets of  $\hat{s}_x$  eigenvalues. Using the tight-binding model, the calculated spin Hall conductivity is quantized to  $\sigma_{yz}^x = (\frac{\hbar}{e}) \frac{G_x e^2}{\pi h}$  with  $G_x$  a reciprocal lattice vector.

## I. INTRODUCTION

Over the past decade, topological materials [1–3] have intrigued many interests in both theory and experiment. Among topological insulators, SOC plays an important role for the nontrivial energy gap. In topological quantum chemistry [4–6], when the phase transition is driven by SOC, we label the transition class by  $(n, m)$ , where  $n$  denotes the number of elementary band representations (eBRs) at the Fermi level ( $E_F$ ) in the absence of SOC while  $m$  denotes the number of derived eBRs in the presence of SOC. In the (2,2)-type, *e.g.*, Bi<sub>2</sub>Se<sub>3</sub>, the phase transition is accidental, and the band inversion depends on the strength of SOC [7–10]. However, in those (1,1)- and (1,2)-types, the gapped phases driven by infinitesimal SOC are topologically nontrivial, corresponding to a topological metal-insulator transition without ‘band inversion’.

Here are three examples for this topological phase transition with no band inversion. The first one is graphene (or silicene), where the Dirac semimetal phase originates from the half filling of the eBR  $A_1@2b$  (SG 183;  $p_z$  orbital) without SOC. Infinitesimal SOC gaps its Dirac point [Fig. 1(a)] and makes it a QSH insulator [11]. The second one is bismuthene on a SiC substrate [12]. The  $p_z$  states are far below  $E_F$  due to its strong coupling with the substrate, while the low-energy bands near  $E_F$  forms the eBR  $E@2b$  (SG 183;  $p_{x,y}$  orbitals) with half filling.

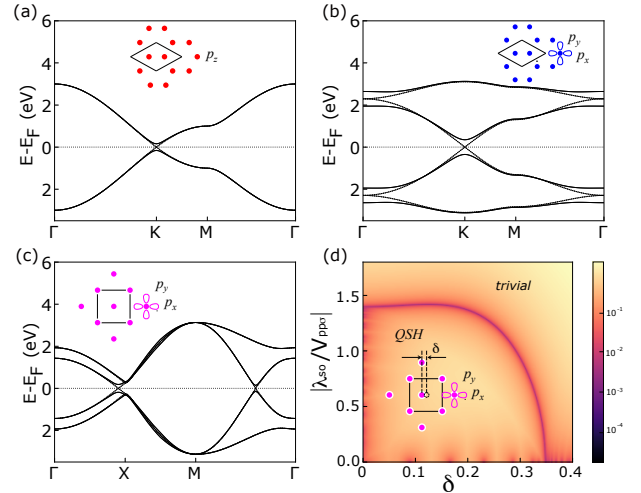


FIG. 1. (color online). The band structures of different lattice models with a topological metal-insulator transition by infinitesimal SOC. Dashed/solid lines are bands without/with SOC. (a)  $p_z$  orbitals on a honeycomb lattice of (1,1)-type. (b)  $p_{x,y}$  or  $d_{xz,yz}$  orbitals on a honeycomb lattice of (1,1)-type. (c)  $p_{x,y}$  orbitals on a square lattice of (1,2)-type. (d) The phase diagram of a distorted square-net layer indicated by the energy gap.

It becomes a QSH insulator with SOC as well [Fig. 1(b)]. The third one is the family of square-net materials, which have attracted lots of attention since the discovery of the anisotropic Dirac fermions in CaMnBi<sub>2</sub> [13, 14]. In an  $X$  square-net compound, the key feature of its band structure (BS) is the half-filling eBR  $E@2a$  (SG 129;  $p_{x,y}$  or-

\* sdx@iphy.ac.cn

† wzj@iphy.ac.cn

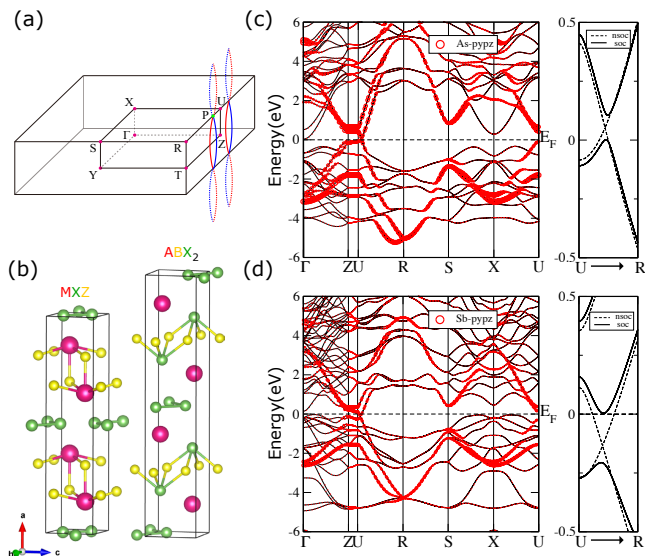


FIG. 2. (color online). The crystal structures, BSs and the Brillouin zone (BZ) of the  $MXZ$  and  $ABX_2$  compounds. (a) The BZ and twisted nodal wires. Each wire consists two non-contractible nodal lines touching a fourfold degenerate point. (b) Crystal structures of the corresponding compounds. Each unit cell contains two distorted  $X$  square-net layers. (c) Orbital-resolved BSs of  $Pnma$  PrAsS without SOC. (d) Orbital-resolved BSs of  $Pnma$  EuCdSb<sub>2</sub> without SOC. The right panels of figures (c) and (d) indicate the band crossings along U–R disappear when SOC is taken into consideration.

bitals). The SOC effect leads the square-net layer into QSH phase [Fig. 1(c)]. Unfortunately, the SOC-induced topological gap is usually rather small in these square-net compounds [15].

In this work, in distorted square-net compounds of  $MXZ$  (LaAsS-family) and  $ABX_2$  (SrZnSb<sub>2</sub>-family) [16–18], the Jahn-Teller effect enlarges the nontrivial gap, which reduces the density of states at  $E_F$ . We propose these compounds with distorted  $X$  square-net layers resemble three-dimensional (3D) QSH effect. In the absence of SOC, the system is a nodal-line semimetal with two twisted nodal wires. Each wire consists of two non-contractible  $\mathcal{TI}$ -protected nodal lines touching at a fourfold degenerate point. Once SOC is included, it becomes a topological crystalline insulator (TCI) with symmetry indicators (SIs)  $(z_2 z_2 z_2; z_4) = (000; 2)$  and  $M_y$  mirror Chern numbers (MCNs)  $(m_0, m_\pi) = (0, 0)$ . With a spectrum gap between two sets of  $\hat{s}_x$  eigenvalues, its nontrivial nature is characterized by a generalized spin Chern number (SCN)  $C_{s+} = 2$ . The 3D QSH effect shall be expected in thin films of insulating candidates, such as CeAs<sub>1+x</sub>Se<sub>1-y</sub> and EuCdSb<sub>2</sub>. Using our tight-binding (TB) model, the calculated spin Hall conductivity (SHC) is quantized, *i.e.*,  $\sigma_{yz}^x = (\frac{\hbar}{e}) \frac{G_x e^2}{\pi h}$  (with  $G_x$  a reciprocal lattice vector).

## II. CALCULATIONS AND RESULTS

*Crystal structures.* The  $MXZ$  and  $ABX_2$  compounds host an orthorhombic lattice (parameters  $a, b, c$  in  $\hat{x}, \hat{y}, \hat{z}$  directions respectively), which is a distorted structure of SG 129 (doubling the unit cell in  $\hat{x}$  direction). As illustrated in Fig. 2(b), each unit cell contains two  $X$  layers ( $x = 0$  and  $0.5a$ ), which are slightly distorted square nets ( $yz$  planes, parametrized by the displacement  $\delta \cdot c$  in  $\hat{z}$  direction). Thus, the zigzag chains are formed along  $\hat{y}$  direction, resulting in the  $X^{1-}$  state.

*Twisted nodal wires in the absence of SOC.* From the orbital-resolved BSs of paramagnetic PrAsS and EuCdSb<sub>2</sub> in Figs. 2(c,d), the key valence and conduction bands are mainly contributed by the  $X$ - $p_{y,z}$  states of the distorted square nets. Detailed calculations show that it is a nodal-line semimetal with two twisted nodal wires. Each nodal wire consists of two non-contractible nodal lines traversing BZ, denoted by the red and blue lines in Fig. 2(a). With time reversal symmetry ( $\mathcal{T}$ ) and inversion symmetry ( $\mathcal{I}$ ), the twofold degenerate nodal lines are protected by the combined anti-unitary symmetry with  $(\mathcal{TI})^2 = 1$ . Hereafter, we focus on the discussion of PrAsS in the main text. More results and details are presented in the Supplemental Material (SM) [19]. In PrAsS, the two non-contractible nodal lines cross each other at P ( $\frac{\pi}{a}, k_y^c = 0.0355 \frac{2\pi}{b}, \frac{\pi}{c}$ ) on the U–R line, leading to an unprecedented twisted nodal wire. The computed irreducible representations (irreps) show that the crossing point P is accidentally fourfold degenerate, formed by two two-dimensional irrep bands (P1P2 and P3P4) with different  $\tilde{C}_{2y} (\equiv \{C_{2y} | 0 \frac{1}{2} 0\})$  eigenvalues [20].

*Nontrivial topology in the presence of SOC.* Upon including SOC, the two twisted nodal wires become fully gapped. The SIs  $(z_2 z_2 z_2; z_4)$  [21] are then computed to be  $(000; 2)$ , indicating a TCI phase [22]. Furthermore, MCNs  $(m_0, m_\pi)$  can be defined in  $k_y = 0$  and  $k_y = \pi/b$  planes with  $M_y (\equiv \mathcal{I} \tilde{C}_{2y})$  symmetry. Using the one-dimensional (1D) Wilson loop method, they are calculated to be  $(m_0, m_\pi) = (0, 0)$  [Figs. S5(a,b) in SM E]. In addition, the hourglass invariant defined by the glide mirror operation  $g_z (\equiv \{\mathcal{I} C_{2z} | \frac{1}{2} 0 \frac{1}{2}\})$  is calculated to be 1 [Figs. S5(c,d) in SM E]. Therefore, we can expect the existence of the hourglass-shaped surface states [23] on  $(010)$  surface.

*QSH phase in the distorted X square net.* The BS of a distorted  $X$  square net ( $xy$  plane) can be simply simulated by a  $p_{x,y}$ -based model with Slater-Koster parameters  $V_{pp\sigma}, V_{pp\pi}$ , displacement  $\delta$ , and SOC strength  $\lambda_{so}$  (SM C). According to the phase diagram (*i.e.*,  $|V_{pp\pi}/V_{pp\sigma}| \sim 0.3$  for Sb) in Fig. 1(d), the QSH phase stands within a large area near the origin. It shows that a small distortion  $\delta$  (Jahn-Teller effect) enlarges the nontrivial gap for a given  $\lambda_{so}$  (*e.g.*,  $0.15|V_{pp\sigma}|$ ). The nearest-neighbor hopping parameters are extracted from first-principles calculations (Table S4 in SM F).

*Minimum tight-binding model of the bulk.* The non-

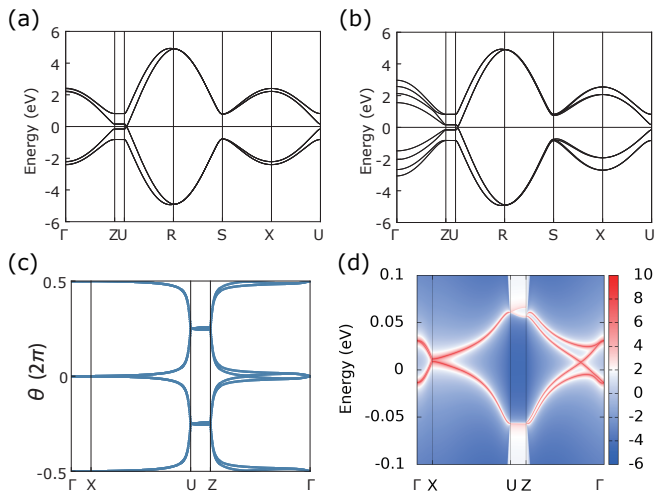


FIG. 3. (color online). BSs and surface states of the minimum TB model. (a) BS without SOC. (b) BS with SOC. (c) The evolution of Wannier charge centers (the  $k_y$ -directed Wilson loops) along  $\bar{\Gamma}X\bar{U}Z\bar{\Gamma}$  in the (010)-surface BZ. (d) (010)-surface spectrum. The hourglass-shaped surface states are presented on  $\bar{\Gamma}\bar{X}$ .

trivial band topology of  $MXZ$  and  $ABX_2$  compounds with and without SOC can be reproduced by two distorted  $X$  square-net layers ( $yz$  planes) with  $p_{y,z}$  orbitals. Details of this TB model are given in SM D. Its BSs [Fig. 3(a,b)] without and with SOC are similar with the  $p_{y,z}$ -fatted bands [Fig. 2(c,d)]. Using `ir2tb` [20] and `Check Topological Mat` [22], the SIs are computed to be (000;2). The  $M_y$  MCNs and  $g_z$  invariant are computed by the 1D Wilson loop method, which are identical with those of PrAsS from first-principles calculations. As we expected, the hourglass-shaped surface states are obtained [24] in the (010)-surface spectrum [Fig. 3(d)].

**3D QSH effect in  $MXZ$  and  $ABX_2$  compounds.** Since the interlayer coupling is weak due to the large distance  $d$  between distorted  $X$  square-net layers (*e.g.*,  $\sim 9$  Å in PrAsS and 11 Å in EuZnSb<sub>2</sub>), one can simply consider the  $MXZ$  and  $ABX_2$  compounds as a stacking of QSH layers [25, 26]. We notice that in real materials, there could be two difficulties in observing the 3D QSH effect experimentally. First, the bulk states could be metallic, when the small QSH gap is messed out by other trivial bands. However, there are a large family of these compounds sharing same band topology [Fig. S1 and Table S1 in SM B], which allows us to adopt various chemical doping. In particular, crystals of CeAs<sub>1+x</sub>Se<sub>1-y</sub> and EuCdSb<sub>2</sub> compounds with an insulating behavior have been synthesized successfully in  $Pnma$  structure [27, 28].

Second, the  $f$  electrons from  $M$  or  $A$  atoms can introduce bothersome magnetism to the systems. Nevertheless, the  $\mathcal{T}$ -broken QSH effect has been proposed in the magnetism-weak-coupling limit [29]. The key point is that the transition from ( $\mathcal{T}$ -broken) QSH phase to a trivial insulator state cannot happen without closing the band gap. Since the  $f$  electrons are quite localized and

far below  $E_F$  (*i.e.*, weakly coupled with the  $X$ - $p$  electrons), we believe that the  $\mathcal{T}$ -broken QSH effect can be realized in those magnetism-weak-coupling compounds. Here, we generalize the SCN defined in Ref. [29] to multiple band systems (even with magnetism). As long as a spectrum gap exists between two sets of  $\hat{s}_x$  eigenvalues, the SCN ( $C_{s+/-}$ ) is well-defined for the positive/negative set. The nontrivial topology can then be described by the generalized SCNs. For each  $k_x$ -fixed plane,  $C_{s\pm} = \pm 2$  can be computed by the 1D Wilson loop method. The results  $k_x = 0$  and  $k_x = \pi/a$  are presented in Figs. 4(a,b).

We propose that such 3D QSH effect can be realized in insulating crystals of these two families. The TB Hamiltonian fully respects the symmetry and topology of corresponding materials, which is crucial to compute the intrinsic SHC. Based on this TB model, we employed the Kubo formula approach at the clean limit to calculate the SHC [30, 31] of this TB model.

$$\sigma_{\alpha\beta}^{\gamma} = \frac{e}{\hbar} \sum_n \int_{\text{BZ}} \frac{d\mathbf{k}}{(2\pi)^3} f_n(\mathbf{k}) \Omega_{\alpha\beta;n}^{\gamma}(\mathbf{k}), \quad (1)$$

$$\Omega_{\alpha\beta;n}^{\gamma}(\mathbf{k}) = 2i\hbar^2 \sum_{m \neq n} \frac{\langle u_{\mathbf{k}}^n | \hat{J}_{\alpha}^{\gamma} | u_{\mathbf{k}}^m \rangle \langle u_{\mathbf{k}}^m | \hat{v}_{\beta} | u_{\mathbf{k}}^n \rangle}{(\varepsilon_{\mathbf{k}}^n - \varepsilon_{\mathbf{k}}^m)^2}$$

where  $\hat{J}_{\alpha}^{\gamma} = \frac{1}{2} \{ \hat{v}_{\alpha}, \hat{s}_{\gamma} \}$  is the spin current operator, with  $\hat{s}$  the spin operator,  $\hat{v}_{\alpha} = \frac{\partial H}{\hbar \partial k_{\alpha}}$  the velocity operator, and  $\alpha, \beta, \gamma = x, y, z$ .  $f_n(\mathbf{k})$  is the Fermi-Dirac distribution.  $|u_{\mathbf{k}}^n\rangle$  and  $\varepsilon_{\mathbf{k}}^n$  are the eigenvectors and eigenvalues of Hamiltonian  $h(\mathbf{k})$ , respectively. The distribution  $\sum_n f_n(\mathbf{k}) \Omega_{yz;n}^x(\mathbf{k})$  in  $k_x = \pi/a$  plane is presented in Fig. 4(c). The SHC, exhibiting quantization, is calculated to be  $\sigma_{yz}^x = \left(\frac{\hbar}{e}\right) \frac{2e^2}{h} \frac{G_x}{2\pi}$  with the chemical potential  $\mu$  in the bulk gap [Fig. 4(d)]. Here,  $G_x$  is the  $\hat{x}$ -component of a reciprocal lattice vector.

### III. DISCUSSION

Besides  $MXZ$  and  $ABX_2$  compounds, the distorted  $X$  square net as a QSH layer can be widely found in material database, including some superconductors, *e.g.*, the 112 family of iron pnictides Ca<sub>1-x</sub>La<sub>x</sub>FeAs<sub>2</sub> [25, 32] and CaSb<sub>2</sub> [33, 34]. The combination of nontrivial band topology and superconductivity may serve a platform for the search of intrinsic topological superconductivity and Majorana zero modes [35–37].

In summary, we find that the distorted  $X$  square-net layers in  $MXZ$  and  $ABX_2$  compounds are QSH layers and the nontrivial topology relies on the  $p_{y,z}$  orbitals of  $X$  atoms. These compounds can be simply considered as a stacking of QSH layers along  $\hat{x}$  direction. Without SOC, the system hosts two twisted nodal wires, each of which contains two non-contractible nodal lines, crossing each other at a fourfold degenerate point. Once SOC is taken into consideration, it becomes a TCI with SIs (000;2) and MCNs (0,0). In the magnetism-weak-coupling limit,

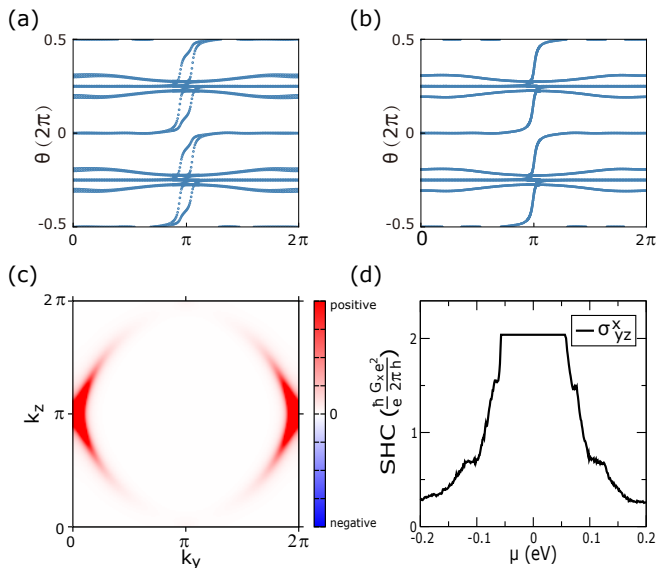


FIG. 4. (color online). The evolution of Wannier charge centers (WCCs) in the positive-eigenvalue set of  $\hat{s}_x$  for bulk PrAsS at (a)  $k_x = 0$  and (b)  $k_x = \pi/a$  planes, suggesting  $C_{s+} = +2$ . Note that the Wilson bands in  $k_x = \pi/a$  plane host  $\tilde{C}_{2x}(\equiv \{C_{2x} | \frac{1}{2} \frac{1}{2} \frac{1}{2}\})\mathcal{T}$ -protected twofold degeneracy. (c) The distribution of  $\sum_n f_n(\mathbf{k}) \Omega_{yz;n}^x(\mathbf{k})$  in  $k_x = \pi/a$  plane. (d) The calculated SHC  $\sigma_{yz}^x$  as a function of chemical potential  $\mu$ .

the nontrivial topology is characterized by the generalized SCNs  $C_{s\pm} = \pm 2$ . The 3D QSH effect in these layered materials has been suggested by the calculated SHC of the corresponding TB model, which are very promising in the insulating compounds, like  $\text{CeAs}_{1+x}\text{Se}_{1-y}$  and  $\text{EuCdSb}_2$ .

## ACKNOWLEDGMENTS

This work was supported by the National Natural Science Foundation of China (Grants No. 11974395, U2032204), the Strategic Priority Research Program of Chinese Academy of Sciences (Grant No. XDB33000000), and the Center for Materials Genome. Changming Yue was supported by the Swiss National Science Foundation (SNF Grant 200021-196966). H.W. acknowledges support from the Science Challenge Project (No. TZ2016004), the K. C. Wong Education Foundation (GJTD-2018-01).

- 
- [1] M. Z. Hasan and C. L. Kane, *Rev. Mod. Phys.* **82**, 3045 (2010).
- [2] X.-L. Qi and S.-C. Zhang, *Rev. Mod. Phys.* **83**, 1057 (2011).
- [3] N. P. Armitage, E. J. Mele, and A. Vishwanath, *Rev. Mod. Phys.* **90**, 015001 (2018).
- [4] B. Bradlyn, L. Elcoro, J. Cano, M. G. Vergniory, Z. Wang, C. Felser, M. I. Aroyo, and B. A. Bernevig, *Nature* **547**, 298 (2017).
- [5] B. Bradlyn, L. Elcoro, M. G. Vergniory, J. Cano, Z. Wang, C. Felser, M. I. Aroyo, and B. A. Bernevig, *Phys. Rev. B* **97**, 035138 (2018).
- [6] S. Nie, Y. Qian, J. Gao, Z. Fang, H. Weng, and Z. Wang, *Phys. Rev. B* **103**, 205133 (2021).
- [7] H. Zhang, C. X. Liu, X. L. Qi, X. Dai, Z. Fang, and S. C. Zhang, *Nat. Phys.* **5**, 438 (2009).
- [8] D. Hsieh, Y. Xia, D. Qian, L. Wray, J. H. Dil, F. Meier, J. Osterwalder, L. Patthey, J. G. Checkelsky, and N. P. Ong, *Nature* **460**, 1101 (2009).
- [9] Y. Xia, D. Qian, D. Hsieh, L. Wray, A. Pal, H. Lin, A. Bansil, D. Grauer, Y. S. Hor, R. J. Cava, and M. Z. Hasan, *Nat. Phys.* **5**, 398 (2009).
- [10] Y. L. Chen, J. G. Analytis, J.-H. Chu, Z. K. Liu, S.-K. Mo, X. L. Qi, H. J. Zhang, D. H. Lu, X. Dai, Z. Fang, S. C. Zhang, I. R. Fisher, Z. Hussain, and Z.-X. Shen, *Science* **325**, 178 (2009).
- [11] C.-C. Liu, W. Feng, and Y. Yao, *Phys. Rev. Lett.* **107**, 076802 (2011).
- [12] F. Reis, G. Li, L. Dudy, M. Bauernfeind, S. Glass, W. Hanke, R. Thomale, J. Schäfer, and R. Claessen, *Science* **357**, 287 (2017).
- [13] Y. Wang, Y. Qian, M. Yang, H. Chen, C. Li, Z. Tan, Y. Cai, W. Zhao, S. Gao, Y. Feng, S. Kumar, E. F. Schwier, L. Zhao, H. Weng, Y. Shi, G. Wang, Y. Song, Y. Huang, K. Shimada, Z. Xu, X. J. Zhou, and G. Liu, *Phys. Rev. B* **103**, 125131 (2021).
- [14] S. Klemenz, S. Lei, and L. M. Schoop, *Annual Review of Materials Research* **49**, 185 (2019).
- [15] Q. Xu, Z. Song, S. Nie, H. Weng, Z. Fang, and X. Dai, *Phys. Rev. B* **92**, 205310 (2015).
- [16] F. Hulliger, R. Schmelzger, and D. Schwarzenbach, *Journal of Solid State Chemistry* **21**, 371 (1977).
- [17] L. Hoistad Strauss and C. M. Delp, *Journal of Alloys and Compounds* **353**, 143 (2003).
- [18] G. Lee, M. A. Farhan, J. S. Kim, and J. H. Shim, *Phys. Rev. B* **87**, 245104 (2013).
- [19] Supplemental Material.
- [20] J. Gao, Q. Wu, C. Persson, and Z. Wang, *Computer Physics Communications* **261**, 107760 (2021).
- [21] Z. Song, T. Zhang, Z. Fang, and C. Fang, *Nature Communications* **9**, 3530 (2018).
- [22] M. G. Vergniory, L. Elcoro, C. Felser, N. Regnault, B. A. Bernevig, and Z. Wang, *Nature* **566**, 480 (2019).
- [23] Z. Wang, A. Alexandradinata, R. J. Cava, and B. A. Bernevig, *Nature* **532**, 189 (2016).
- [24] Q. Wu, S. Zhang, H.-F. Song, M. Troyer, and A. A. Soluyanov, *Computer Physics Communications* **224**, 405 (2018).
- [25] X. Wu, S. Qin, Y. Liang, C. Le, H. Fan, and J. Hu, *Phys. Rev. B* **91**, 081111 (2015).

- [26] Y. Qian, Z. Tan, T. Zhang, J. Gao, Z. Wang, Z. Fang, C. Fang, and H. Weng, *Science China Physics, Mechanics & Astronomy* **63** (2020), 10.1007/s11433-019-1515-4.
- [27] A. Schlechte, R. Niewa, Y. Prots, W. Schnelle, M. Schmidt, and R. Kniep, *Inorganic Chemistry*, 2277 (2009).
- [28] M. Ohno, M. Uchida, Y. Nakazawa, S. Sato, M. Kriener, A. Miyake, M. Tokunaga, Y. Taguchi, and M. Kawasaki, *APL Materials* **9**, 051107 (2021).
- [29] Y. Yang, Z. Xu, L. Sheng, B. Wang, D. Y. Xing, and D. N. Sheng, *Phys. Rev. Lett.* **107**, 066602 (2011).
- [30] Y. Zhang, Y. Sun, H. Yang, J. Železný, S. P. P. Parkin, C. Felser, and B. Yan, *Phys. Rev. B* **95**, 075128 (2017).
- [31] D. Xiao, M.-C. Chang, and Q. Niu, *Rev. Mod. Phys.* **82**, 1959 (2010).
- [32] N. Katayama, K. Kudo, S. Onari, T. Mizukami, K. Sugawara, Y. Sugiyama, Y. Kitahama, K. Iba, K. Fujimura, N. Nishimoto, M. Nohara, and H. Sawa, *Journal of the Physical Society of Japan* **82**, 123702 (2013), <https://doi.org/10.7566/JPSJ.82.123702>.
- [33] H. Takahashi, S. Kitagawa, K. Ishida, M. Kawaguchi, A. Ikeda, S. Yonezawa, and Y. Maeno, *Journal of the Physical Society of Japan* **90**, 073702 (2021), <https://doi.org/10.7566/JPSJ.90.073702>.
- [34] K. Funada, A. Yamakage, N. Yamashina, and H. Kageyama, *Journal of the Physical Society of Japan* **88**, 044711 (2019), <https://doi.org/10.7566/JPSJ.88.044711>.
- [35] X. Wu, W. A. Benalcazar, Y. Li, R. Thomale, C.-X. Liu, and J. Hu, *Phys. Rev. X* **10**, 041014 (2020).
- [36] Z. Wang, P. Zhang, G. Xu, L. K. Zeng, H. Miao, X. Xu, T. Qian, H. Weng, P. Richard, A. V. Fedorov, H. Ding, X. Dai, and Z. Fang, *Phys. Rev. B* **92**, 115119 (2015).
- [37] S. Nie, L. Xing, R. Jin, W. Xie, Z. Wang, and F. B. Prinz, *Phys. Rev. B* **98**, 125143 (2018).
- [38] G. Kresse and D. Joubert, *Phys. Rev. B* **59**, 1758 (1999).
- [39] J. P. Perdew, K. Burke, and M. Ernzerhof, *Phys. Rev. Lett.* **77**, 3865 (1996).
- [40] H. J. Monkhorst and J. D. Pack, *Phys. Rev. B* **13**, 5188 (1976).

## APPENDIX

## A. Calculation methods

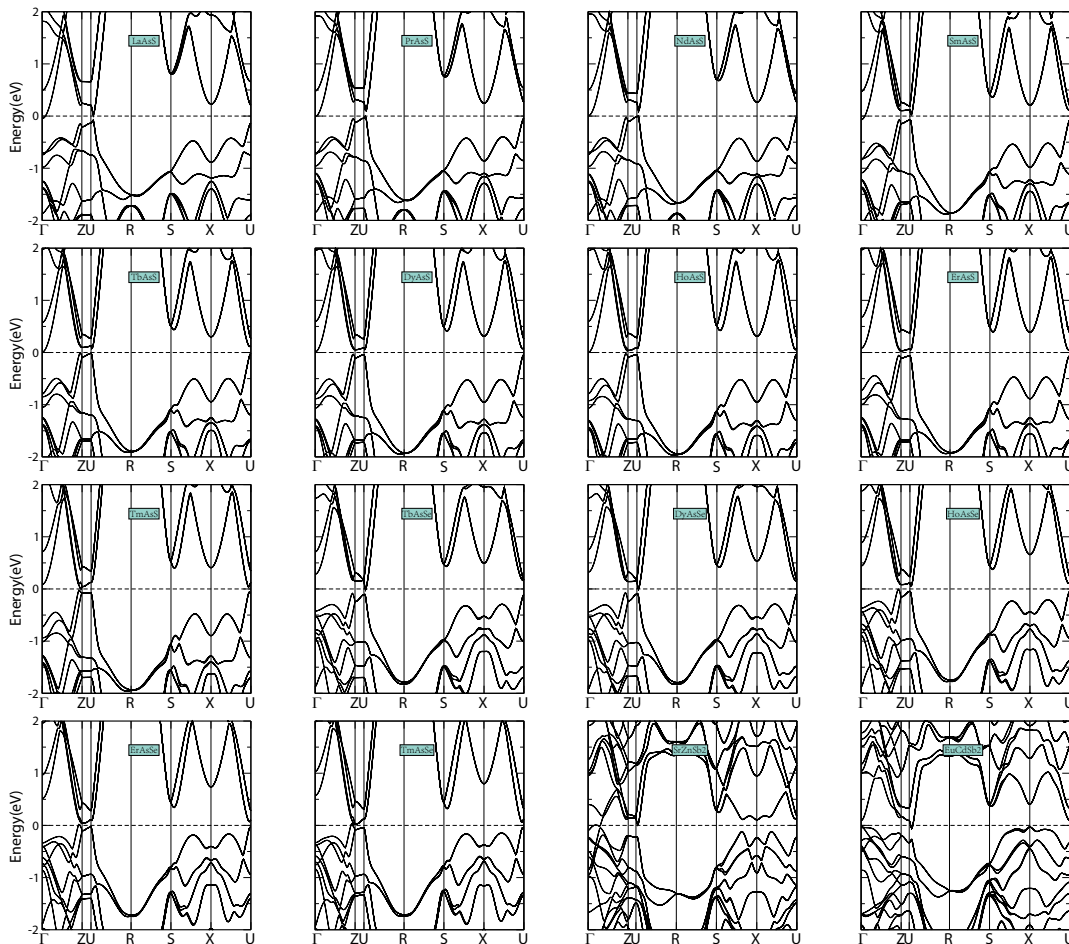
We performed first-principles calculations based on the density functional theory (DFT) using projector augmented wave (PAW) method implemented in the Vienna ab initio simulation package (VASP) [38]. The generalized gradient approximation (GGA) as implemented in the Perdew-Burke-Ernzerhof (PBE) functional [39] was adopted. The cutoff parameter for the wave functions was 520 eV. The BZ was sampled by Monkhorst-Pack method [40] with  $4 \times 10 \times 10$  for the 3D periodic boundary condition. The  $f$  electrons in lanthanide are neglected in our calculations.

B. BSs of LaAsS- and SrZnSb<sub>2</sub>- family compounds

As listed in Table S1 and the corresponding BSs with SOC shown in Fig. S1, there exists a large family (LaAsS- and SrZnSb<sub>2</sub>- family) compounds sharing similar BSs and same band topology.

TABLE S1. LaAsS- and SrZnSb<sub>2</sub>- family compounds with similar BSs and the same topological nature.

| $(z_2 z_2 z_2; z_4)$ | Compounds |       |        |        |        |        |        |        |                     |
|----------------------|-----------|-------|--------|--------|--------|--------|--------|--------|---------------------|
| (000; 2)             | LaAsS     | PrAsS | HoAsS  | ErAsS  | TmAsS  | TbAsS  | DyAsS  | HoAsS  | SrZnSb <sub>2</sub> |
|                      | NdAsS     | SmAsS | HoAsSe | ErAsSe | TmAsSe | TbAsSe | DyAsSe | HoAsSe |                     |

FIG. S1. (color online). BSs of the LaAsS- and SrZnSb<sub>2</sub>- families with same band topology.

### C. Phase diagram of the distorted square net

The distorted  $X$  square-net monolayer consists of two  $X$  atoms locating at  $A : (0, 0)$  and  $B : (1/2 - \delta, 1/2)$  in a unit cell (lattice constant  $l$ ). The parameter  $\delta$  describes the distortion, as shown in the main text and Fig. S2. TB model of such a distorted square net is constructed by the  $p_{x,y}$  orbitals of the two  $X$  atom. We consider only the nearest-neighboring (NN) hopping (bond 1) and next-nearest-neighboring (NNN) hopping (bond 2 in Fig. S2) in our TB model, which is enough to capture the phase transition between the QSH phase and trivial insulator.

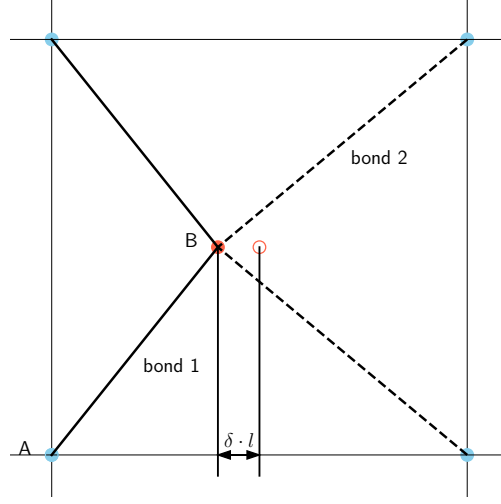


FIG. S2. (color online). Structure of a distorted  $X$  square-net layer, with blue and red cycles representing two sub-lattices, respectively. Black solid line denotes the NN hopping (bond 1;  $d_1^2 = [l/2]^2 + [l/2 - \delta \cdot l]^2$ ), while black dashed line denotes the NNN hopping (bond 2;  $d_2^2 = [l/2]^2 + [l/2 + \delta \cdot l]^2$ ).

According to the distance ( $d$ ) of the bonds (*i.e.*,  $d_1$  for bond 1 and  $d_2$  for bond 2), we parametrize the Slater-Koster (SK) hopping strength in a uniform way,  $V_i(d) \equiv \frac{l^2}{2d^2} V_i$ ,  $i \in \{pp\sigma, pp\pi\}$ .

First, we introduce the operator

$$\psi_{\mathbf{k}}^\dagger \equiv \psi_{\mathbf{k},\uparrow}^\dagger \oplus \psi_{\mathbf{k},\downarrow}^\dagger; \quad \psi_{\mathbf{k},s}^\dagger \equiv (c_{A,x,s}^\dagger(\mathbf{k}), c_{A,y,s}^\dagger(\mathbf{k}), c_{B,x,s}^\dagger(\mathbf{k}), c_{B,y,s}^\dagger(\mathbf{k})), \quad (\text{S1})$$

where  $c_{b,\alpha,s}^\dagger(\mathbf{k})$  is the fermionic creation operator with  $b \in \{A, B\}$ ,  $\alpha \in \{p_x, p_y\}$ , and  $s \in \{\uparrow, \downarrow\}$ , which denotes sub-lattice ( $A$  and  $B$ ), orbital ( $p_x$  and  $p_y$ ), and spin (up and down), respectively. The TB Hamiltonian  $H_{tb} = H_0 + H_{so}$  can then be written as (expressed under basis  $\psi_{\mathbf{k}}$ , *i.e.*,  $\{\uparrow, \downarrow\} \otimes \{A, B\} \otimes \{p_x, p_y\}$ )

$$\begin{aligned} H_{tb} &= H_0 + H_{so} \\ &= \sum_{\mathbf{k}} \psi_{\mathbf{k}}^\dagger [s_0 \otimes h_0(\mathbf{k}) + h_{so}] \psi_{\mathbf{k}} \end{aligned} \quad (\text{S2})$$

Here, the matrix  $h_{so}$  denotes the atomic SOC term of  $X$  atoms, which reads,

$$h_{so} = \lambda_{so} s_z \otimes \tau_0 \otimes \sigma_y \quad (\text{S3})$$

with  $\lambda_{so}$  the strength of SOC, while  $\mathbf{s}$ ,  $\boldsymbol{\tau}$  and  $\boldsymbol{\sigma}$  are Pauli matrices in spin, sub-lattice, and orbital space, respectively. While the Hermitian matrix  $h_0(\mathbf{k})$  can be expressed as

$$h_0(\mathbf{k}) = \begin{pmatrix} h_{13}(\mathbf{k}) & h_{14}(\mathbf{k}) \\ h_{23}(\mathbf{k}) & h_{24}(\mathbf{k}) \\ \dagger & \dagger \\ \dagger & \dagger \end{pmatrix} \quad (\text{S4})$$

where the matrix elements  $h_{\beta\beta'}$ ,  $\beta \in \{1, 2, 3, 4\} \equiv \{A, B\} \otimes \{p_x, p_y\}$ , are given by

$$\begin{aligned} h_{13}(\mathbf{k}) &= \left( 2t_1^{13} e^{i(\frac{1}{2}-\delta)k_x} + 2t_2^{13} e^{-i(\frac{1}{2}+\delta)k_x} \right) \cos \frac{k_y}{2}, \\ h_{24}(\mathbf{k}) &= \left( 2t_1^{24} e^{i(\frac{1}{2}-\delta)k_x} + 2t_2^{24} e^{-i(\frac{1}{2}+\delta)k_x} \right) \cos \frac{k_y}{2}, \\ h_{14}(\mathbf{k}) = h_{23}(\mathbf{k}) &= \left( 2it_1^{14} e^{i(\frac{1}{2}-\delta)k_x} + 2it_2^{14} e^{-i(\frac{1}{2}+\delta)k_x} \right) \sin \frac{k_y}{2}, \end{aligned} \quad (\text{S5})$$

Here,  $t_j^{\beta\beta'}$ ,  $j \in \{1, 2\}$  corresponds to two kinds of bond, which can be obtained through SK method based on the data from first-principle calculations.

$$\begin{aligned} t_1^{13} &= \left( \frac{l/2}{d_1} \right)^2 V_{pp\pi}(d_1) + \left( \frac{l/2 - \delta l}{d_1} \right)^2 V_{pp\sigma}(d_1) \\ t_2^{13} &= \left( \frac{l/2}{d_2} \right)^2 V_{pp\pi}(d_2) + \left( \frac{l/2 + \delta l}{d_2} \right)^2 V_{pp\sigma}(d_2) \\ t_1^{24} &= \left( \frac{l/2}{d_1} \right)^2 V_{pp\sigma}(d_1) + \left( \frac{l/2 - \delta l}{d_1} \right)^2 V_{pp\pi}(d_1) \\ t_2^{24} &= \left( \frac{l/2}{d_2} \right)^2 V_{pp\sigma}(d_2) + \left( \frac{l/2 + \delta l}{d_2} \right)^2 V_{pp\pi}(d_2) \\ t_1^{14} &= \frac{l/2}{d_1} \frac{l/2 - \delta l}{d_1} [V_{pp\sigma}(d_1) - V_{pp\pi}(d_1)] \\ t_2^{14} &= \frac{l/2}{d_2} \frac{l/2 + \delta l}{d_2} [V_{pp\sigma}(d_2) - V_{pp\pi}(d_2)] \end{aligned} \quad (\text{S6})$$

#### D. Minimum tight-binding model for the distorted compounds in SG 62

According to the projected BSs shown in Fig. 2(c,d), we find that the key bands near  $E_F$  are contributed by the  $X - p_{y,z}$  orbitals. Furthermore, the band inversion near  $U$  which brings the nontrivial topology can be well depicted within these states. Thus, we can simplify our analysis within a sixteen-band (spinful) TB model based on  $p_{y,z}$  orbitals of 4  $X$  atoms, locating at the  $4c(m)$  Wyckoff positions of SG 62 [A:  $(x, 1/4, z)$ , B:  $(1-x, 3/4, 1-z)$ , C:  $(-x+1/2, 3/4, z+1/2)$ , and D:  $(x+1/2, 1/4, -z+1/2)$ ]. The crystal structure is shown in FIG. S3. Parameter  $z$  can be viewed as the small distortions along  $\hat{c}$  direction (distortion of square-net layers). Only 5 kinds of bonds between As atoms have been considered in the model, denoted as  $E_i$ ,  $i \in \{1, 2, \dots, 5\}$  in FIG. S3.

TABLE S2. The fitted parameters of TB model for SG 62 lattice structure, with atoms locating at  $4c(m)$  Wyckoff positions.

| $i$ | $V_{pp\sigma}^i, V_{pp\pi}^i$ (eV) | $\lambda_{yy,\uparrow\downarrow}^i$ (eV) | $\lambda_{yz,\uparrow\downarrow}^i$ (eV) | $\lambda_{zz,\uparrow\downarrow}^i$ (eV) |
|-----|------------------------------------|--|--|--|
| 1   | 2.09000, -0.77000                  |  | 0.08 <i>i</i>                            |  |
| 2   | 1.53000, -0.54000                  |  | 0.07 <i>i</i>                            |  |
| 3   | 0.00936, -0.00187                  | 0.003 <i>i</i>                           | 0.001 <i>i</i>                           | 0.002 <i>i</i>                           |
| 4   | 0.00807, -0.00161                  | 0.04 + 0.02 <i>i</i>                     | 0.05 + 0.03 <i>i</i>                     | 0.07 + 0.05 <i>i</i>                     |
| 5   | 0.00726, -0.00145                  | 0.03 + 0.01 <i>i</i>                     | 0.04 + 0.02 <i>i</i>                     | 0.06 + 0.04 <i>i</i>                     |

Similarly to Sec. C, we first construct the basis

$$\psi_{\mathbf{k}}^{\dagger} \equiv \psi_{\mathbf{k},\uparrow}^{\dagger} \oplus \psi_{\mathbf{k},\downarrow}^{\dagger}; \quad \psi_{\mathbf{k},s}^{\dagger} \equiv \left( c_{A,y,s}^{\dagger}(\mathbf{k}), c_{A,z,s}^{\dagger}(\mathbf{k}), \dots, c_{D,y,s}^{\dagger}(\mathbf{k}), c_{D,z,s}^{\dagger}(\mathbf{k}) \right) \quad (\text{S7})$$

where  $c_{b,\alpha,s}^{\dagger}(\mathbf{k})$  is the fermionic creation operator with  $b \in \{A, B, C, D\}$ ,  $\alpha \in \{p_y, p_z\}$ , and  $s \in \{\uparrow, \downarrow\}$  being sub-lattice, orbital, and spin indices, respectively. Therefore, the TB Hamiltonian  $H'_{tb} = H'_0 + H'_{so}$  can be written as (expressed under basis  $\psi_{\mathbf{k}}^{\dagger}$ , *i.e.*,  $\{\uparrow, \downarrow\} \otimes \{A, B, C, D\} \otimes \{p_y, p_z\}$ )

$$\begin{aligned} H'_{tb} &= H'_0 + H'_{so} \\ &= \sum_{\mathbf{k}} \psi_{\mathbf{k}}^{\dagger} [s_0 \otimes h'_0(\mathbf{k}) + h'_{so}(\mathbf{k})] \psi_{\mathbf{k}} \end{aligned} \quad (\text{S8})$$

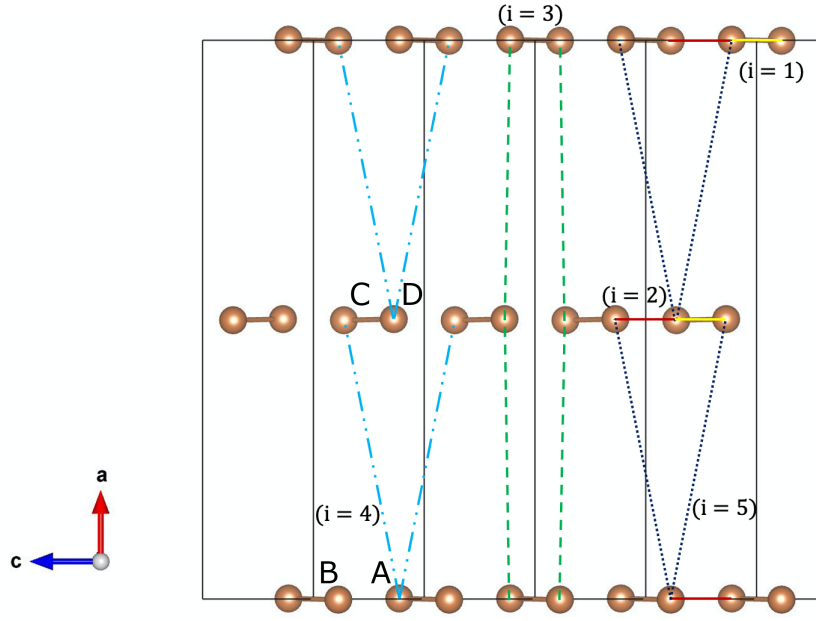


FIG. S3. (color online). Lattice structure of TB model and 5 kinds of bonds, with yellow solid line being  $E_1$ , red solid line being  $E_2$ , green dashed line being  $E_3$ , blue dashed line being  $E_4$ , and purple dashed line being  $E_5$ .

TABLE S3. Representations of SG 62 generators and TR operation

|            | $\mathcal{T}$                                   | $\tilde{C}_{2z}$   | $\tilde{C}_{2y}$   | $\mathcal{I}$  |
|------------|---|--|--|--|
| $(ijk; b)$ | $(ijk; b)$                                      | $(ijk; A) \mapsto (\bar{i}jk; C) + (\bar{1}\bar{1}0)$<br>$(ijk; B) \mapsto (\bar{i}jk; D) + (\bar{1}\bar{1}\bar{1})$<br>$(ijk; C) \mapsto (\bar{i}jk; A) + (\bar{1}\bar{1}\bar{1})$<br>$(ijk; D) \mapsto (\bar{i}jk; B) + (\bar{1}\bar{1}0)$ | $(ijk; A) \mapsto (\bar{i}jk; B) + (10\bar{1})$<br>$(ijk; B) \mapsto (\bar{i}jk; A) + (\bar{1}\bar{1}\bar{1})$<br>$(ijk; C) \mapsto (\bar{i}jk; D) + (\bar{1}\bar{1}\bar{1})$<br>$(ijk; D) \mapsto (\bar{i}jk; C) + (\bar{1}0\bar{1})$ | $(ijk; A) \mapsto (\bar{i}jk; B) + (\bar{1}\bar{1}\bar{1})$<br>$(ijk; B) \mapsto (\bar{i}jk; A) + (\bar{1}\bar{1}\bar{1})$<br>$(ijk; C) \mapsto (\bar{i}jk; D) + (\bar{1}\bar{1}\bar{1})$<br>$(ijk; D) \mapsto (\bar{i}jk; C) + (\bar{1}\bar{1}\bar{1})$ |
| $\alpha$   | $\begin{pmatrix} 1 & 0 \\ 0 & 1 \end{pmatrix}$  | $\begin{pmatrix} -1 & 0 \\ 0 & 1 \end{pmatrix}$  | $\begin{pmatrix} 1 & 0 \\ 0 & -1 \end{pmatrix}$  | $\begin{pmatrix} -1 & 0 \\ 0 & -1 \end{pmatrix}$   |
| $s$        | $\begin{pmatrix} 0 & -1 \\ 1 & 0 \end{pmatrix}$ | $\begin{pmatrix} -i & 0 \\ 0 & i \end{pmatrix}$  | $\begin{pmatrix} 0 & -1 \\ 1 & 0 \end{pmatrix}$  | $\begin{pmatrix} 1 & 0 \\ 0 & 1 \end{pmatrix}$   |

where the matrix  $h'_{so}(\mathbf{k})$  reads,

$$h'_{so}(\mathbf{k}) = h'_{so,0} + h'_{so,1}(\mathbf{k}) \quad (\text{S9})$$

in which the atomic SOC term  $h'_{so,0} = \lambda'_{so} s_x \otimes \mathbb{I}_{4 \times 4} \otimes \sigma_y$ , with  $\lambda'_{so} = 0.08\text{eV}$  the atomic SOC strength,  $\mathbb{I}_{4 \times 4}$  the identity matrix in sub-lattice space,  $\mathbf{s}$  and  $\boldsymbol{\sigma}$  the Pauli matrices in spin and orbital space, respectively.

All other hopping terms can be derived from those listed in Table S2, with symmetry generators (*i.e.*,  $\tilde{C}_{2z}$ ,  $\tilde{C}_{2y}$  and  $\mathcal{I}$ ) of SG 62 and time-reversal (TR) operator  $\mathcal{T}$ . In general, we can label an arbitrary As atom by  $(ijk; b)$ , with Miller indices  $(ijk)$  and  $b \in \{A, B, C, D\}$ . Any symmetry operator  $R$  in SG 62 maps As  $(ijk; b)$  to another  $(i'j'k'; b')$ , *i.e.*,  $R : (ijk; b) \mapsto (i'j'k'; b')$ . The concrete representations of these operators in orbital ( $\alpha$ ) and spin ( $s$ ) space, *i.e.*,  $R : c_{\alpha(s)}^\dagger \mapsto \sum_{\alpha'(s')} c_{\alpha'(s')}^\dagger \mathcal{U}(R)_{\alpha'\alpha(s's)}$ , are listed in Table S3.

### E. The evolution of WCCs for $M_y$ MCNs and hourglass invariant $g_z$

To characterize the topological properties in the PrAsS system,  $M_y$  MCNs ( $m_0, m_\pi$ ) and the hourglass invariant  $g_z$  are calculated by the 1D Wilson loop method. As shown in Fig. S5(a,b),  $M_y$  MCNs are calculated to be (0,0) in  $k_y = (0, \pi/b)$  planes. Similarly,  $g_z$  invariant and SCNs in  $k_x = (0, \pi/a)$  planes are calculated to be 1 [Fig. S5(c,d)] and (2,2) [Fig. 4(a,b) in the main text].

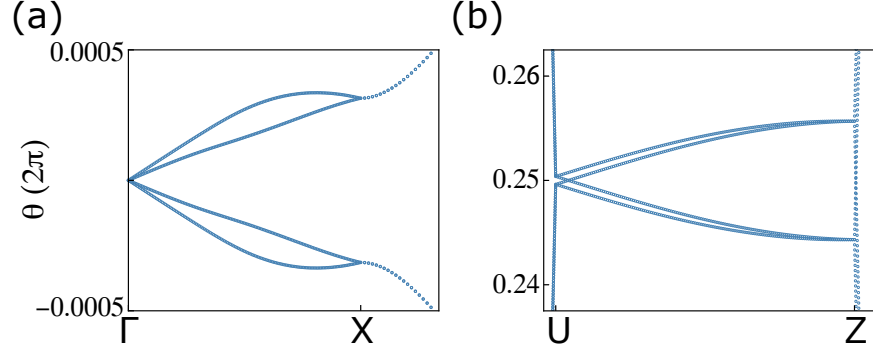


FIG. S4. (color online). Close-ups of the Wilson band along (a)  $\Gamma$ -X and (b) U-Z.

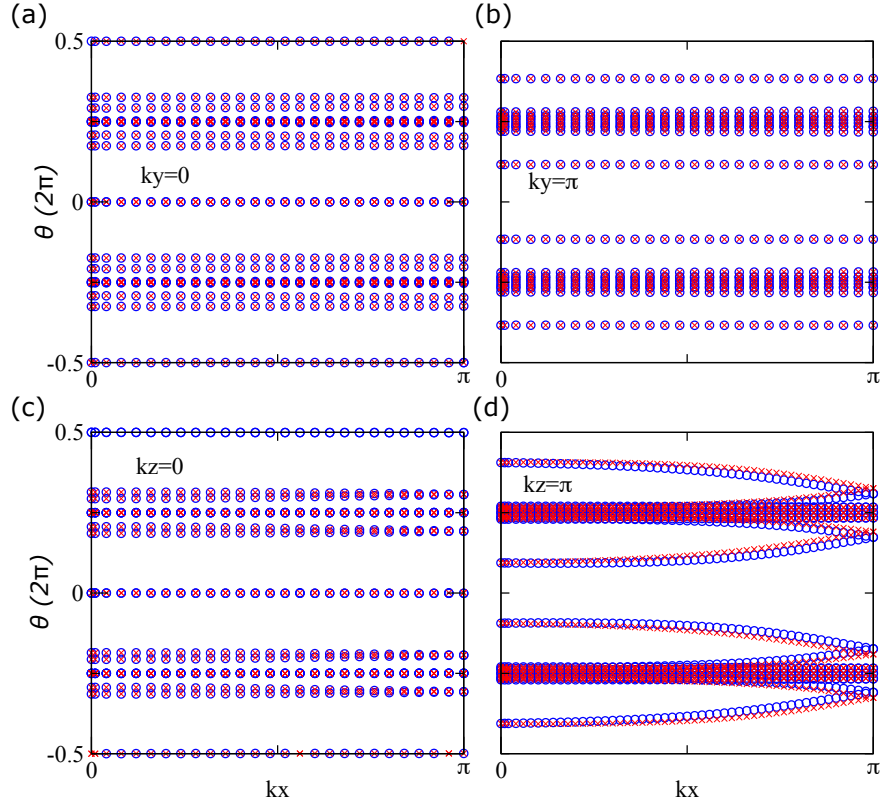


FIG. S5. (color online).  $k_z$ - and  $k_y$ - directed Wilson loop spectra of bulk PrAsS. MCNs at (a)  $k_y = 0$  plane and (b)  $k_y = \pi/b$  plane.  $g_z$ , *i.e.*, the hourglass-shaped evolution of  $k_z$ -directed Wilson loop on the (c)  $\Gamma$ -X line and (d) U-Z line.

### F. DFT bands of a $X$ square-net layer

Using hopping parameters listed in Table S4, BSs from the TB model recover the orbital-resolved BSs near  $E_F$  from the first-principles calculations, *i.e.*, the fitted TB model captures the topological features in distorted  $X$  square-net monolayers.

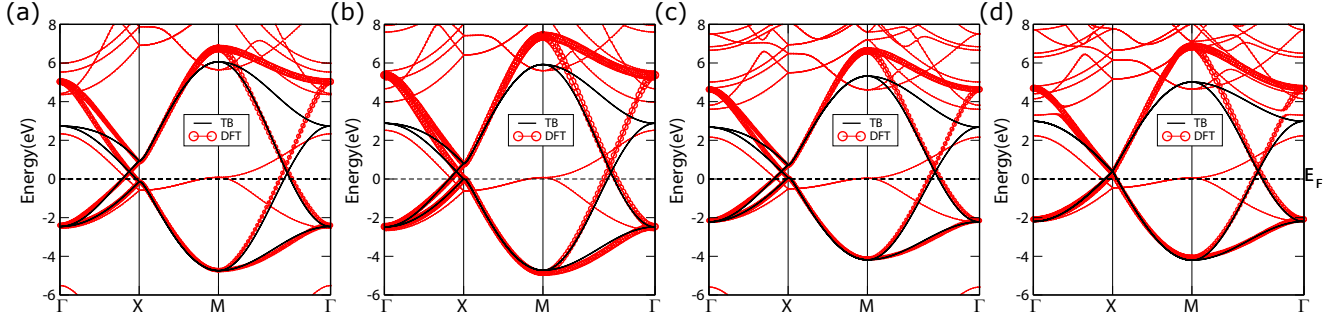


FIG. S6. (color online). The orbital-resolved BSs of  $X$  square-net monolayers without SOC from DFT (labeled by “DFT” in the legend), the size of red cycles represents the weight of  $X$ - $p_{x,y}$  orbitals. The BSs of fitted TB model is shown by black lines.

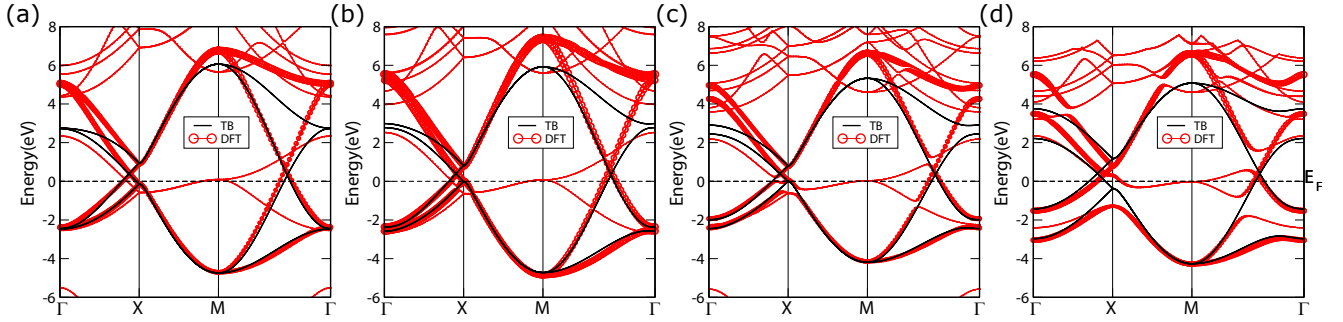


FIG. S7. (color online). The orbital-resolved BSs of  $X$  square-net monolayers with SOC from DFT (labeled by “DFT” in the legend), the size of red cycles represents the weight of  $X$ - $p_{x,y}$  orbitals. The BSs of fitted TB model is shown by black lines.

TABLE S4. The fitted parameters from the first-principles calculations for an  $X$  square-net layer (lattice constant  $l$ ). The SK parameters for the nearest-neighboring (NN)  $X$ - $X$  bonds are  $V_{pp\sigma}, V_{pp\pi}$ , and those of the next-nearest-neighboring (NNN)  $X$ - $X$  bonds are  $V'_{pp\sigma}, V'_{pp\pi}$ .

| $X$ | $l$ (Å) | $V_{pp\sigma}, V_{pp\pi}$ (eV) | $V'_{pp\sigma}, V'_{pp\pi}$ (eV) | $V_{pp\sigma}/V_{pp\pi}$ | $\lambda_{so}$ (eV) | Example             |
|-----|---------|--------------------------------|----------------------------------|--------------------------|---------------------|---------------------|
| P   | 3.8     | -2.0, 0.700                    | -0.40, 0.1400                    | -0.35                    | 0.020               | GdPS                |
| As  | 3.9     | -2.0, 0.660                    | -0.30, 0.0990                    | -0.33                    | 0.105               | PrAsS               |
| Sb  | 4.4     | -1.8, 0.576                    | -0.25, 0.0800                    | -0.32                    | 0.230               | EuCdSb <sub>2</sub> |
| Bi  | 4.5     | -1.8, 0.504                    | -0.01, 0.0028                    | -0.28                    | 0.770               | CaMnBi <sub>2</sub> |